JACS
JOURNAL OF THE AMERICAN CHEMICAL SOCIETY
Article
pubs.acs.org/JACS

Enforcing Multifunctionality: A Pressure-Induced Spin-Crossover Photomagnet

Dawid Pinkowicz,*[,†] Michał Rams,[‡] Martin Mišek,[§,∥] Konstantin V. Kamenev,[⊥] Hanna Tomkowiak,[#] Andrzej Katrusiak,[#] and Barbara Sieklucka[†]

[†]Faculty of Chemistry, Jagiellonian University, Ingardena 3, 30-060 Kraków, Poland
[‡]Institute of Physics, Jagiellonian University, Łojasiewicza 11, 30-348 Kraków, Poland
[§]School of Physics and Astronomy, Centre for Science at Extreme Conditions, University of Edinburgh, Edinburgh EH9 3JZ, United Kingdom
[∥]Institute of Physics ASCR, v.v.i, Na Slovance 2, 182 21 Prague 8, Czech Republic
[⊥]School of Engineering, Centre for Science at Extreme Conditions, University of Edinburgh, Edinburgh EH9 3FD, United Kingdom
[#]Faculty of Chemistry, Adam Mickiewicz University, Umultowska 89b, 61-614 Poznań, Poland

Supporting Information

ABSTRACT: Photomagnetic compounds are usually achieved by assembling preorganized individual molecules into rationally designed molecular architectures via the bottom-up approach. Here we show that a magnetic response to light can also be enforced in a nonphotomagnetic compound by applying mechanical stress. The nonphotomagnetic cyano-bridged Fe^{II}–Nb^{IV} coordination polymer $\{[Fe^{II}(pyrazole)_4]_2[Nb^{IV}(CN)_8]\cdot 4H_2O\}_n$ (**FeNb**) has been subjected to high-pressure structural, magnetic and photomagnetic studies at low temperature, which revealed a wide spectrum of pressure-related functionalities including the light-induced magnetization. The multifunctionality of **FeNb** is compared with a simple structural and magnetic pressure response of its analog $\{[Mn^{II}(pyrazole)_4]_2[Nb^{IV}(CN)_8]\cdot 4H_2O\}_n$ (**MnNb**). The **FeNb** coordination polymer is the first pressure-induced spin-crossover photomagnet.

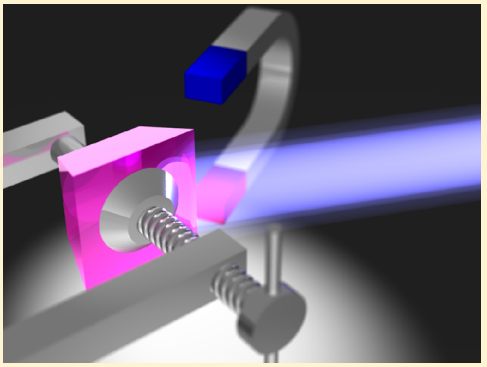

INTRODUCTION

Molecular solids are usually pursued via the bottom-up modular approach and synthesized by assembling properly designed building blocks that are carriers of various functionalities, i.e., ferromagnetism, superparamagentism,[1] quantum nanomagnetism,[2−4] chirality,[5−8] redox activity,[9] luminescence,[10] spin crossover,[11,12] photochromism,[13] photomagnetism,[14−17] conductivity,[18] or piezochromism.[18,19] The occurrence of several selected functionalities within a single compound is called multifunctionality[20,21] and can take the form of a simple coexistence, an interaction, when one function affects the other and enables switching behavior or a cross-coupling leading to new physical and chemical cross-effects of higher order.[5]

Photomagnets constitute a special class of multifunctional materials that either become paramagnetic, ferromagnetic, or distinctly change their magnetic properties upon illumination.[22,23] Since its discovery,[22] photomagnetism has received a lot of attention as it offers a unique way of controlling spins and magnetization by photons, which is not available in conventional magnets (metals and oxides).[24] In other words, light can be used to generate, manipulate, and read out spins.[25] So far two main classes of photomagnetic materials have been investigated: spin crossover[11,15,24,26] and charge-transfer photomagnets.[27] The former class employs the light-induced excited spin-state trapping (LIESST) effect[28] that enables switching between low-spin (LS) and high-spin (HS) states of a single metal center by light. In case of octahedral Fe^{II}, the light wavelength has to fall within the $^1A_1 \rightarrow {}^1T_1$ d−d absorption band of the LS state for LIESST or the $^5T_2 \rightarrow {}^5E$ d−d absorption band of the HS state for reverse-LIESST to occur.[29] Charge-transfer photomagnets[27] work similarly, but the light-induced spin transition is a consequence of an electron transfer between two metal centers. The most intensely explored charge-transfer photomagnets stem from Prussian Blue analogs[30,31] and their 4d and 5d congeners.[32]

An elegant example of a light-induced spin-crossover magnet based on the LIESST effect is the $\{[Fe^{II}(4\text{-pyridinealdoxime})_4][Nb^{IV}(CN)_8]\}\cdot 2H_2O$ three-dimensional (3-D) coordination polymer with cyanide bridges connecting the Fe^{II} and Nb^{IV} centers, reported by Ohkoshi and co-workers.[24] This molecular system shows gradual thermal spin-crossover transition at Fe^{II} centers resulting in a paramagnetic behavior at low-temperature stemming from the remaining $S = 1/2$ Nb^{IV}. The illumination leads to the LIESST effect generating HS ($S = 2$) Fe^{II} centers and activates local antiferromagnetic Fe^{II}–Nb^{IV} interactions

Received: April 25, 2015
Published: June 22, 2015

DOI: 10.1021/jacs.5b04303
J. Am. Chem. Soc. 2015, 137, 8795−8802

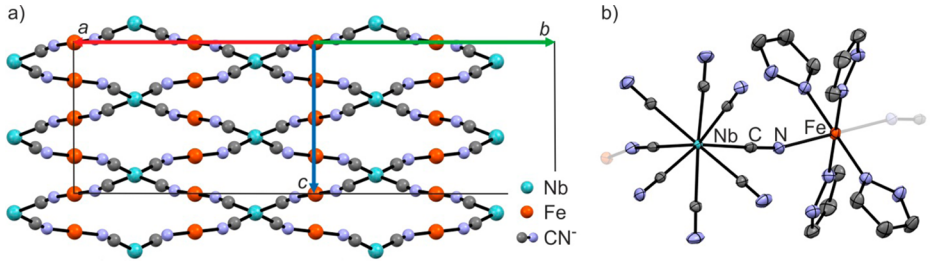

Figure 1. Crystal structure of **FeNb**. (a) The compressed diamond-like topology of the −Nb−CN−Fe−NC− framework (terminal cyanides, pyrazole, and water molecules omitted for clarity). (b) The structure of the −Nb−CN−Fe−NC− motif (H atoms omitted, thermal ellipsoids at the 50% probability level).

between the light-generated HS Fe^{II} and the Nb^{IV} centers. This in turn leads to spontaneous magnetization and light-induced long-range ferrimagnetic ordering at 20 K due to the strong magnetic exchange pathways provided by the 3-D $-Nb^{IV}-CN-Fe^{II}-$ coordination skeleton.

We have studied cyanide-bridged $Fe^{II}-Nb^{IV}$ systems since our report on the first iron(II)-octacyanoniobate(IV) ferromagnet in 2009.[33] Similarly as Ohkoshi et al.,[34] we aimed at $Fe^{II}-Nb^{IV}$ spin-crossover compounds with photoinduced ferromagnetic state, without much success at that time. However, the analysis of these results[33,35] indicated the potential of high-pressure experiments[36−39] unexplored for $\{[Fe^{II}(pyrazole)_4]_2[Nb^{IV}(CN)_8]\cdot 4H_2O\}_n$ (**FeNb**)[35] and led to the observation of a pressure-induced spin-crossover phenomenon reported herein. During these studies, we realized that LIESST effect should be also possible at high pressure, and we conceived a high-pressure photomagnetic experiment that would confirm this hypothesis. Here we report the first example of a pressure-induced spin-crossover photomagnet **FeNb** exhibiting various magnetic and photomagnetic phenomena under pressure and the first successful high-pressure photomagnetic experiment. The pressure- and temperature-dependent magnetic properties of **FeNb** include the magnetic ordering (ferrimagnetism and antiferromagnetism), pressure-induced and thermal-induced spin-crossover transition, and photomagnetism. It also shows a pronounced spin-crossover-related piezochromic behavior. The pressure-induced spin-crossover is confirmed by single-crystal X-ray diffraction (sc-XRD) structural analysis under pressure at room temperature and is further supported by high-pressure Raman spectroscopy. Additionally, the pressure-induced magnetic and structural properties of **FeNb** are confronted with its manganese(II) analogue $\{[Mn^{II}(pyrazole)_4]_2[Nb^{IV}(CN)_8]\cdot 4H_2O\}_n$ (**MnNb**), where neither spin-crossover nor related photomagnetic phenomena occur.

RESULTS AND DISCUSSION

FeNb has a diamond-like polymeric structure (tetragonal $I4_1/a$) strongly converged along the c direction with Nb^{IV} and Fe^{II} centers linked together through slightly bent cyanide bridges (Figure 1a and animation 1 in Supporting Information). The $-Nb^{IV}-CN-Fe^{II}-NC-$ structural motif (Figure 1b) repeats in a 3-D cyanide-based framework, with the compressed pseudotetrahedral Nb^{IV} nodes connected to four Fe^{II} midpoint centers of linear linkers. The Nb^{IV} are eight-coordinate with CN^- ligands arranged in a dodecahedral spatial geometry, while the Fe^{II} centers are octahedral, with two axially N-coordinated CN^- ligands and four pyrazole ligands in the equatorial plane (Figure 1b).

Hydrostatic compression of **FeNb** in a Merrill−Bassett diamond-anvil cell (DAC) results in dramatic structural changes, which were determined by sc-XRD (see Table S1 in the Supporting Information for crystallographic details). The structural data under pressure obtained for **FeNb** are compared with the respective pressure-induced structural deformations in the manganese(II) analogue **MnNb** (see Table S2 in Supporting Information for crystallographic details). The observed changes in **FeNb** include a considerable volume compression (−15.4% at 2.36 GPa compared to −12.4% at 2.42 GPa for **MnNb**; Figure 2a) and the Fe−N bonds shrinkage typical for HS−LS Fe^{II} spin-crossover transition: for $Fe-N_{CN}$

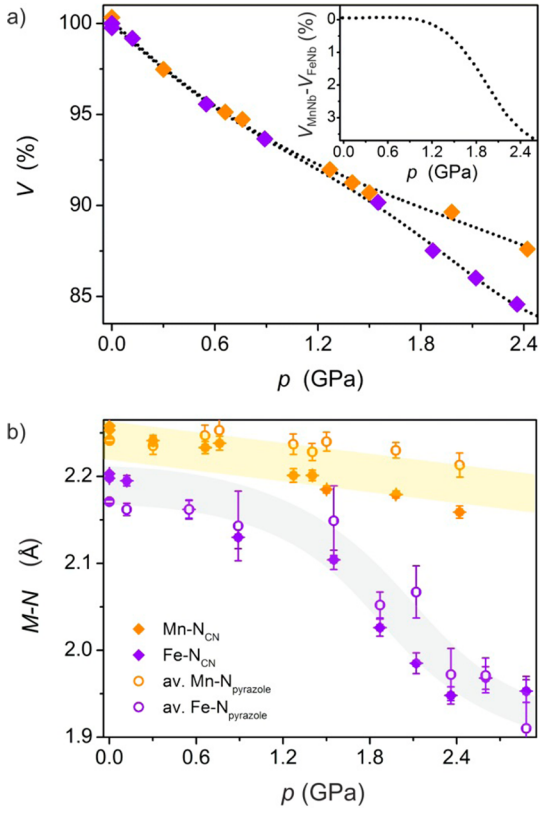

Figure 2. Structural changes in **FeNb** and **MnNb** versus pressure. (a) Normalized unit-cell volume for **MnNb** (orange points) and **FeNb** (purple points) with the lines representing the best polynomial fits as guides for the eye (errors are smaller than the symbols; volumes under high pressure are normalized to the volume at ambient pressure). (inset) The difference between normalized unit-cell volumes of **MnNb** and **FeNb**. (b) Pressure dependence of the M−N bond lengths for **MnNb** (orange) and **FeNb** (purple) highlighted for guiding the eye.

DOI: 10.1021/jacs.5b04303
J. Am. Chem. Soc. 2015, 137, 8795−8802

from 2.198(3) Å at ambient pressure to 1.953(13)Å at 2.88 GPa and for Fe−$N_{pyrazole}$ from 2.171(2)Å at 0.1 MPa to 1.91(6)Å at 2.88 GPa (Figure 2b and Figure S1, Table S3, and animation 2 in Supporting Information). The increased standard deviations of the Fe−$N_{pyrazole}$ bond lengths in the 0.8−2.4 GPa range reflect probably the gradual change of the populations of the transformed regions in the crystal, with the coexisting longer (of about 2.15 Å) and shorter (of ca. 1.95 Å) bonds. This would be contrary to the concept of a gradual change in the lengths of these particular bonds, assuming intermediate values during the transition, and could mean that the Fe−N_{CN} bonds behave differently. The respective bond length shrinkage in **MnNb** is much less pronounced and can be associated with the typical structural response to hydrostatic pressure. The volume compression (Figure 2a) and the shrinkage of the corresponding bonds (Figure 2b) are significantly stronger in **FeNb** than in **MnNb** above around 1.6 GPa, consistently with the pressure-induced spin-crossover transition of the Fe^{II} centers at room temperature.

Noteworthy, the Mn−NC−Nb bridge in **MnNb** is considerably more bent at higher pressures than the corresponding Fe−NC−Nb bridge, which remains basically unchanged (Figure S1, Supporting Information). Such a behavior of **FeNb** partly compensates the severe pressure-induced shrinkage of the Fe^{II} coordination sphere. All structural changes in **MnNb** and **FeNb** are fully reversible as confirmed by full structural analyses of the crystals after releasing the pressure from 0.55 and 5.00 GPa for **FeNb** and from 1.30 GPa for **MnNb** (Tables S1−S3, Supporting Information).

The pressure-induced changes were also followed by recording the Raman spectra in a DAC up to 3.61 GPa at room temperature (Figure 3). From 0.10 MPa to 1.11 GPa a significant hypsochromic shift of the three characteristic cyanide bands[35] occurs (highlighted in red in Figure 3) in line with the gradual bond length reduction within the Nb−CN−Fe_{HS} motif and its bending observed by the XRD structural analysis. At 1.11 and 1.68 GPa two new bands appear with their maxima at 2107 and 2144 cm^{-1} (blue in Figure 3). These new bands are related to the pressure-induced spin crossover at Fe^{II} and can be ascribed to stretching vibrations of the CN^- ligands coordinated to LS Fe^{II} centers. Increasing pressure gradually reduces the multiplet related to the HS Fe^{II} as well as increases the intensity of two LS Fe^{II}-related bands and shifts them toward higher wavenumbers. This confirms that the spin-crossover is induced in compressed **FeNb** and the transition starts around 1.2 GPa.

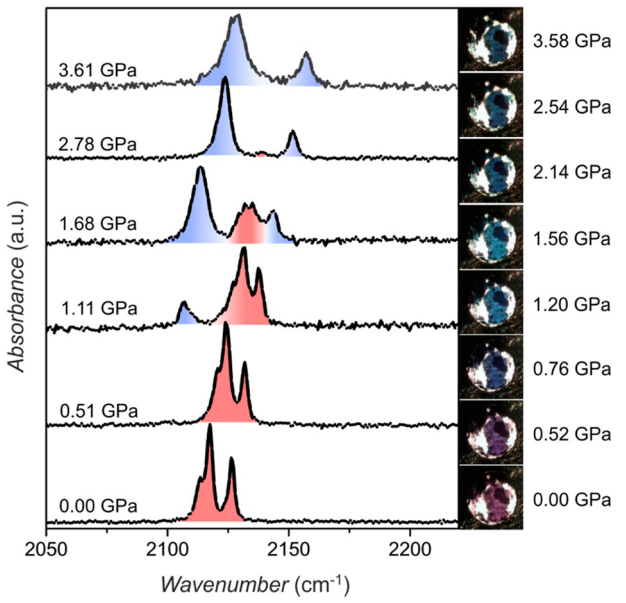

Figure 3. Raman spectra and piezochromism of **FeNb**. The CN-stretching vibration region shows the pressure-induced changes related to the HS (red) to LS (blue) transition of the Fe^{II} centers at room temperature (left). The microphotographs of **FeNb** powder sample under pressure (right panel) demonstrate the piezochromic effect at room temperature.

The changes in the CN-stretching region are fully reversible, which excludes the possibility of the irreversible CN-bridge isomerization (from Nb−CN−Fe to Nb−NC−Fe, see Figure S2, Supporting Information for the Raman spectrum before and after the high pressure experiment).[40] However, the reversible CN-bridge isomerization cannot be ruled out at this point. The **FeNb** exhibits also a pronounced piezochromic behavior caused by the pressure-induced ligand field change at the Fe^{II} centers and the pressure-induced spin-crossover transition. Its color changes form dark pink at ambient pressure, through purple, blue and finally dark blue above 2.0 GPa (Figure 3 and video file in Supporting Information). These studies indicate clearly that mechanical stress causes the spin-crossover transition in **FeNb**.

At ambient pressure and low temperatures, **FeNb** is a ferrimagnet.[35] It exhibits a net ferromagnetic behavior due to the antiferromagnetic coupling between the nonequal neighboring spin carriers: Fe^{II} and Nb^{IV} (Figure 4 and Figure 5). The transition to a long-range magnetic ordered phase occurs at T_c = 9.4 K. Above that temperature (10−300 K range) **FeNb** is a paramagnet with the room temperature χT product of 7.59 cm^3 K mol^{-1} (χ is molar magnetic susceptibility), which is close to the theoretical 7.64 cm^3 K mol^{-1}, assuming noninteracting HS Fe^{II} with S = 2, g_{Fe} = 2.2 and Nb^{IV} with S = 1/2, g_{Nb} = 2.0. The high pressure significantly changes its magnetic behavior. First of all, increasing pressure gradually decreases χT in the whole temperature range and lowers the plateau around 60 K (Figure 4a). These changes are also clearly visible in the $\chi^{-1}(T)$ plots and the obtained Curie constants as a function of pressure (Figure S3 and Table S4, Supporting Information). Moreover, at 0.5 GPa the long-range magnetic order changes from ferrimagnetic to antiferromagnetic, which is manifested by the loss of spontaneous magnetization characteristic for ferrimagnets (ferromagnets) observed at p < 0.5 GPa and the appearance of a maximum in the $M(T)$ dependence at $p \geq$ 0.5 GPa typical for antiferromagnets (Figure 4b inset, Figure 5, and Figure S4, Supporting Information). At higher pressures (p > 0.8 GPa) the transition to an antiferromagnetic phase becomes blurred and disappears above 1.0 GPa (Figure S4, Supporting Information).

The structural analysis and Raman spectra suggests that the observed changes of magnetic properties are due to the pressure-induced spin-crossover transition occurring at Fe^{II} centers.[41] The $\chi T(T)$ curves in the high-temperature region (250−50 K; Figure 4a) indicate that at ambient pressure, all Fe^{II} centers are in the HS state (S = 2; HS Fe^{II}). With increasing pressure, a fraction of Fe^{II} centers undergoes an incomplete thermal spin-crossover transition to the LS diamagnetic state (S = 0; LS Fe^{II}). This manifests itself in the lowering of the magnetic ordering temperature in the 0.3−0.5 GPa region, which might be caused by the magnetic correlation

DOI: 10.1021/jacs.5b04303
J. Am. Chem. Soc. 2015, 137, 8795−8802

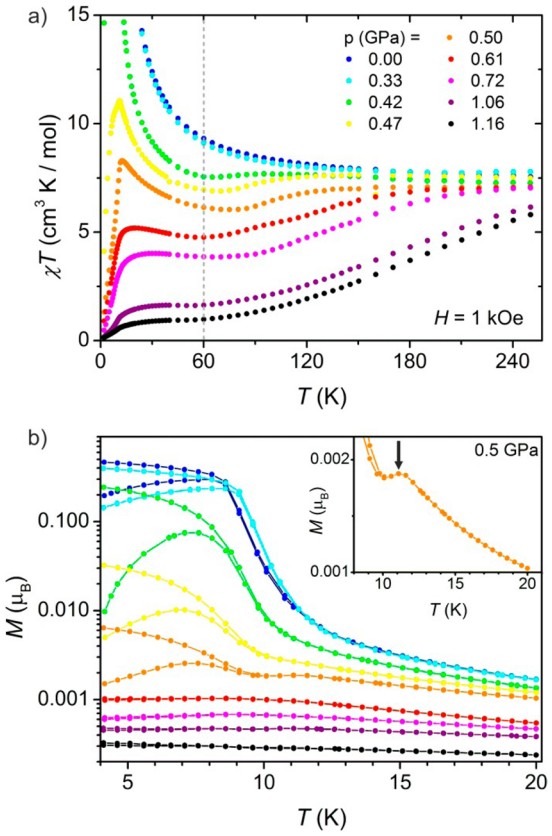

Figure 4. Magnetic properties of **FeNb** under pressure. (a) Molar magnetic susceptibility and temperature product per Fe_2Nb unit measured at 1 kOe upon cooling. (b) Zero-field cooled and field cooled magnetization per Fe_2Nb unit measured at 15 Oe (solid lines are guides to the eye only). (Inset) Magnetization under 0.50 GPa with a maximum at 11.5 K indicating long-range antiferromagnetic ordering.

length becoming restricted (Figure 4b). At 0.5 GPa and below 50 K, the estimated fraction of LS Fe^{II} is 0.25 (Figure S5 and Table S4, Supporting Information). Between 0.5 and 0.8 GPa, the fraction (0.75−0.50; Figure S5, Supporting Information) and the distribution of the remaining HS centers promote the formation of antiferromagnetically coupled magnetic regions separated presumably by a layers of LS Fe^{II} leading to the bulk antiferromagnetic behavior below 11.5 K (Figure 4b inset, Figure 5b, and Figure S5, Supporting Information). At higher pressure (above 1.0 GPa) and low temperature (below 80 K), the spin-crossover transition is almost complete, which leaves weakly coupled Nb^{IV} centers as the only spin carriers. Thus, the magnetic ordering is completely replaced by the paramagnetic behavior (Figure S5, Supporting Information). It can be concluded that the applied pressure determines the fraction of Fe^{II} centers undergoing thermal spin-crossover and the low-temperature magnetic behavior of **FeNb**.

This analysis is further supported by the shape of the magnetization vs. magnetic field curves at 2.0 K (Figure S6, Supporting Information). Below 0.4 GPa the $M(H)$ dependence is characteristic for ferromagnets/ferrimagnets. In the 0.42−0.72 GPa range the $M(H)$ curves become typical for antiferromagnetic/metamagnetic systems with critical fields between 6 and 9 kOe. Above 1.0 GPa the $M(H)$ curves lose the features of the metamagnetic transition. The magnetization at 50 kOe decreases with increasing pressure, which is indirectly related to the fraction of Fe^{II} centers undergoing pressure- and temperature-induced spin-crossover transition.

The comparison of the pressure-dependent magnetic data of **FeNb** and **MnNb** confirms that the observed behavior of **FeNb** is caused by the pressure-induced thermal spin-crossover occurring at Fe^{II} centers resulting in diamagnetic LS Fe^{II}. The magnetic behavior of **MnNb** does not show any features of spin crossover. Curie constants obtained by fitting the $\chi^{-1}(T)$ dependences with the Curie−Weiss law in the 200−300 K range and up to 0.92 GPa do not vary significantly and are only slightly lower than the expected spin-only value of 9.125 cm^3 K mol^{-1} for two $S = 5/2$ Mn^{II} and one $S = 1/2$ Nb^{IV} center assuming $g = 2.00$ (Figure S7, Supporting Information). The analysis of the $M(H)$ curves and the magnetization saturation values at 2.0 K also confirm no pressure effect on the total magnetic moment of the Mn_2Nb unit (Figure S8, Supporting Information). The ferrimagnetic transition at $T_c = 23.4$ K at 0.1 MPa is shifted toward higher temperatures by the applied pressure (Figure S9a, Supporting Information). The T_c increase is linear in the investigated pressure range (up to 1.03 GPa) with the slope $dT_c/dp = 12.4 \pm 0.2$ K·GPa^{-1} (Figure S9b, Supporting Information); similar to that in the previously

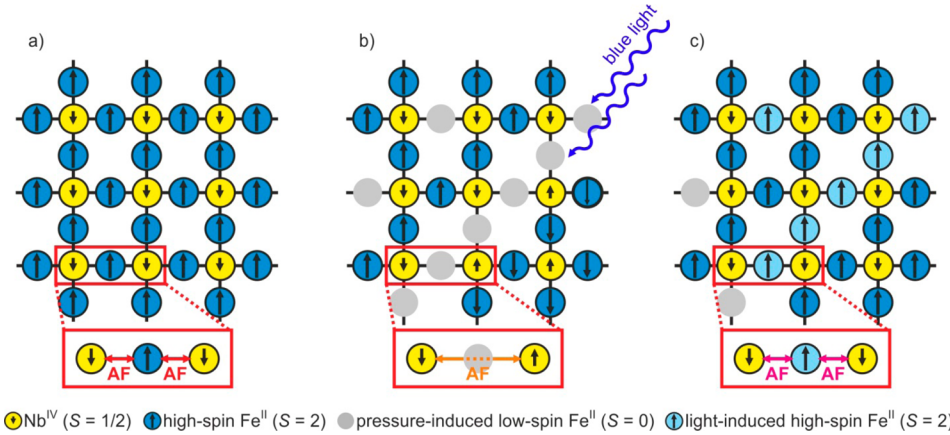

Figure 5. Schematic diagram illustrating the pressure-induced spin-crossover and photomagnetic effect in **FeNb**. Pressure-induced spin-crossover transition leading to LS Fe^{II} centers and the change from a ferrimagnet ($p = 0$ GPa, $T = 2$ K, $H = 100$ Oe; a) to an antiferromagnet ($p = 0.60$ GPa, $T = 2$ K, $H = 100$ Oe; two antiferromagnetically coupled regions are shown; b). The blue light irradiation at high pressure generates HS Fe^{II} states due to the LIESST effect and restores the long-range ferrimagnetic order ($p = 0.60$ GPa, $T = 2$ K, $H = 100$ Oe; c).

DOI: 10.1021/jacs.5b04303
J. Am. Chem. Soc. 2015, 137, 8795−8802

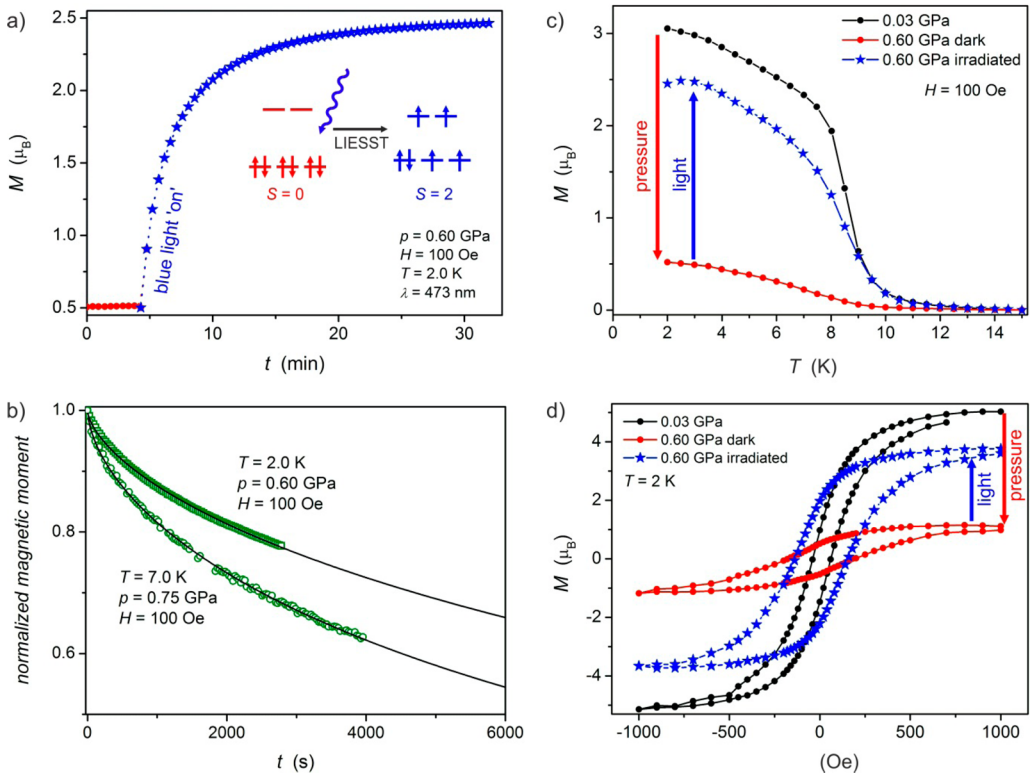

Figure 6. Photomagnetic measurements under pressure for **FeNb**. (a) Magnetization during illumination of the sample at 0.60 GPa. (b) Relaxation of the normalized magnetic moment recorded after switching "off" the light at two different sets of thermodynamic parameters, solid lines represent the best fit to the stretched exponential decay function (squares: T = 2.0, p = 0.60 GPa, H = 100 Oe; circles: T = 7.0 K, p = 0.75 GPa, H = 100 Oe). (c) Magnetization vs temperature at 100 Oe applied DC field at 0.03 GPa (black), 0.60 GPa without light (red), and with continuous light irradiation (blue). (c) Magnetization vs field at 2.0 K at 0.03 GPa (black), 0.60 GPa without light (red), and with continuous light irradiation (blue).

reported Mn^{II}–Nb^{IV} cyanide-bridged system with pyridazine as a coligand.[42] Such a behavior is consistent with the antiferromagnetic exchange transmitted through Nb–CN–Mn bridge. Pressure-induced structural changes, especially the Mn–N bond shrinkage, increase the overlap of the respective orbitals within Nb^{IV}–CN-Mn^{II} structural motif and strengthens the antiferromagnetic interactions.[43,44]

The photomagnetic measurements were performed for **FeNb** under pressure in a turnbuckle magnetic diamond anvil pressure cell (TM-DAC)[45,46] with an optical fiber for sample illumination. The initial measurements "in the dark" at 0.03 and 0.60 GPa confirmed the same pressure-induced magnetic behavior as observed by using the CuBe cell. The transition to the ferrimagnetic phase at 9.4 K at 0.03 GPa was almost completely lost by applying 0.60 GPa pressure. Irradiation of the sample at 0.60 GPa with 473 nm laser light (5 mW power; the choice of the wavelength was based on the observations of Ohkoshi et al.)[24] caused an immediate increase of magnetization by the factor of 2.7 after only 20 min (Figure 6a and Figure 5b,c). The time-dependent experiment was repeated several times for three independent loadings of TM-DAC and slightly different pressures up to 1.0 GPa, leading each time to the same result: a light-induced magnetization (Figure 6 and Figure S10, Supporting Information). Above 1.0 GPa the photomagnetic effect could not be observed anymore, most probably due to the structural restraint of the Fe^{II} sites at higher pressures preventing the occurrence of LIESST. It is important to mention that the photoinduced phase is relaxing slowly back to the initial state (Figure 6b). The relaxation rate has been determined by fitting the time dependence of the normalized magnetic moment $f = (m - m_{dark})/(m_{off} - m_{dark})$ (where m is the measured magnetic moment, m_{dark} is the last magnetic moment value right before switching "on" the irradiation and m_{off} is the value of the magnetic moment immediately after switching the irradiation "off", see Figure S11 in Supporting Information for more details) for two independent loadings at two different sets of temperature, pressure, and magnetic field parameters, using a stretched exponential decay function $f = \exp(-\tau/t)^{\beta}$ which is suitable for gradual spin-crossover systems[47,48] (τ is the average relaxation time, t is the time, and β parameter describes the width of the relaxation time distribution). The obtained best fit parameters are τ_1 = 23 630 ± 270 s, β_1 = 0.639 ± 0.003 (adjusted R^2 = 0.99908) at 2 K, 0.60 GPa, 100 Oe and τ_2 = 13 580 ± 90 s, β_2 = 0.610 ± 0.002 (adjusted R^2 = 0.99914) at 7 K, 0.75 GPa, 100 Oe. This means that the relaxation rate is slow at 2 K, 0.60 GPa (several hours) and a little bit faster at 7 K, 0.75 GPa (few hours). The β parameter of ca. 0.6 indicates that the distribution width of the magnetization relaxation times is broad (the relaxation of the magnetization is not linearly dependent on the fraction of relaxing HS Fe^{II} centers).

The field cooled magnetization vs temperature dependence at 0.6 GPa (Figure 6c) recorded under continuous illumination has a very similar shape to the $M(T)$ curve at 0.03 GPa and very similar critical temperature indicating light-induced long-range magnetic order. Similar conclusion can be drawn from the analysis of the magnetic hysteresis loops recorded at 2 K (Figure 6d). At 0.03 GPa (close to ambient pressure), **FeNb** is a ferrimagnet with a narrow hysteresis loop and magnetization of 5.0 μ_B at 1000 Oe (black points in Figure 6c). Pressure of

DOI: 10.1021/jacs.5b04303
J. Am. Chem. Soc. 2015, 137, 8795–8802

0.60 GPa is sufficient to reduce the magnetization to 1.1 μ_B (red points in Figure 6c). Blue light irradiation at low temperature leads to the anticipated strong photomagnetic response which manifests itself in larger magnetization similar to that observed before pressurizing the sample (blue stars in Figure 6c). The increase of coercive field under pressure is consistent with increasing disorder due to the distribution of HS Fe^{II}. Figure S10 (in the Supporting Information) presents the aforementioned results in a more detailed way which includes zero-field cooled and field cooled magnetization plots. Magnetic measurements without continuous illumination show some signs of magnetization relaxation that reduces slightly the long-range magnetic ordering temperature and the magnetization of the photoinduced ferrimagnetic phase (green stars in Figure S10d, Supporting Information). This confirms the photoinduced spontaneous magnetization under pressure. Even after several hours the relaxation was only slight and each time the magnetization stabilized at 200−250% of the initial level, depending on the TM-DAC loading.

The light- and pressure-induced changes are fully reversible; heating the sample back to room temperature and releasing the pressure back to ambient restores completely the initial state (Figure S10b, Supporting Information). The analysis of the photoinduced magnetic phase shows that blue light restores the long-range magnetic order in the compressed **FeNb** by regenerating HS Fe^{II} ($S = 2$) centers due to the LIESST effect (Figure 5). The restored magnetic exchange within the $-Nb^{IV}-CN-Fe^{II}-$ skeleton results in the photoinduced ferrimagnetically ordered phase.

CONCLUSIONS

The first pressure-induced photomagnetic effect has been demonstrated by performing high-pressure magnetic measurements up to 1.0 GPa with simultaneous illumination of the sample. The experiment revealed that the cyano-bridged **FeNb** compound is the pressure-induced spin-crossover photomagnet, which exhibits multifunctional behavior enforced by mechanical stress. This study shows that complex magnetic behavior including a variety of intriguing properties can be induced by properly adjusting the thermodynamic conditions. **FeNb** does not exhibit spin-crossover and photomagnetic behavior at ambient conditions but becomes multifunctional after adjusting the pressure. The presented approach to multifunctionality by manipulating temperature, pressure, and light is the first example of such a level of solid matter control that forces the photomagnetic switching. It is a new concept that can be adapted to other potentially photoactive molecular solids, opening a new field of high-pressure photomagnetic materials.

EXPERIMENTAL SECTION

Synthesis. $\{[Fe^{II}(pyrazole)_4]_2[Nb^{IV}(CN)_8]\cdot 4H_2O\}_n$ and $\{[Mn^{II}(pyrazole)_4]_2[Nb^{IV}(CN)_8]\cdot 4H_2O\}_n$ in the form of crystalline powders and single crystals were synthesized in an aqueous solution using building block approach according to literature procedure.[35] All reagents for the syntheses, except $K_4[Nb^{IV}(CN)_8]\cdot 2H_2O$,[49] were purchased from commercial sources. The purity of the samples was confirmed by elemental analysis and powder X-ray diffraction experiments. Both **MnNb** and **FeNb** were identical in all respects to those reported in the ref 33.

High-Pressure Single-Crystal XRD Structural Analysis. The experiments were performed on single-crystal samples loaded into a modified Merrill−Bassett high-pressure diamond anvil-cell (DAC).[50] Crystals were glued to the anvil culet. Fluorinert oil was used as a pressure-transmitting medium. Pressure in the DAC sample chamber was determined with an accuracy of 0.03 GPa by the ruby-fluorescence method using a Photon Control Inc. spectrometer.[51] Pressure was checked before and after each diffraction experiment. The single-crystal data were measured using the KUMA KM4-CCD diffractometer at 296 K. Data collection and preliminary data reduction were performed with the CrysAlis software package. Intensities of reflections were corrected for the DAC absorption, gasket shadowing, and the sample absorption.[52,53] Reflections overlapping with diamond reflections were excluded. All structures were solved using direct methods and refined anisotropically using weighted full-matrix least-squares on F^2.[54] Details of the diffraction experiments and crystal data are given in the Supporting Information (Table S1 for **FeNb** and Table S2 for **MnNb**, Table S3, and Figure S1). All structures were deposited at the Cambridge Crystallographic Data Centre and have been assigned the following numbers: CCDC 1054045−1054065. These data can be obtained free of charge via www.ccdc.cam.ac.uk/data_request/cif.

High-Pressure Raman Spectroscopy. Raman spectra were collected for **FeNb** sample sealed in a standard Merrill−Bassett DAC at room temperature using Jobin-Yvon Labram Raman microscope equipped with 633 nm He−Ne laser.

High-Pressure Magnetic Measurements. Magnetic measurements under pressure were carried out using Quantum Design MPMS-XL5 (**FeNb**) and MPMS3 (**MnNb**) magnetometers. The samples in form of crystalline powders were loaded into the CuBe piston-cylinder-type high-pressure capsule cell (HPCC; manufactured by HMD, Japan). Daphne 7373 oil was used as a pressure-transmitting medium hydrostatic up to 1.2 GPa. The actual pressure in the sample chamber at low temperature was determined with 0.02 GPa accuracy from the linear pressure dependence of the superconducting transition of high-purity lead ($dT_c/dp = 0.379$ K/GPa) in case of **MnNb** and the pressure dependence of the superconducting transition of high-purity tin ($dT_c/dp = 0.489$ K/GPa) in case of **FeNb** (AC susceptibility, 0.3 Oe, 1 Hz). The residual field of the MPMS magnet was canceled before each measurement. The magnetic data for both compounds were corrected for the background of the pressure cell filled with oil. The curves of the SQUID voltage response vs sample position in the gradiometer for **FeNb** were fitted taking into account the subtracted background. In case of **MnNb**, where the signal is much stronger, a simple subtraction of the HPCC measured magnetic moment was sufficient.

High-Pressure Photomagnetic Measurements. For photomagnetic measurements under high pressure, a unique combination of a MPMS Fiberoptic Sample Holder (FOSH; Quantum Design) and a turnbuckle magnetic diamond anvil pressure cell (TM-DAC)[45,46] was used. The experimental setup consisted of the TM-DAC placed in a standard straw holder attached to the modified FOSH. Optical fiber and the quartz rod of the FOSH providing the incident 473 ± 1 nm laser light (MBL-III-473 powered by PSU-III-LED power supply) were attached to the cell, and a similar piece of quartz rod was attached to its bottom in order to minimize the asymmetry of the experimental setup and its influence on the gradiometer response vs sample position curves. All measurements have been corrected for the background signal of the empty pressure cell. Daphne 7373 oil was used as a pressure transmitting medium. A small amount of **FeNb** (ca. 10 μg, estimated from comparison with the magnetization data of the bulk sample) was loaded into TM-DAC together with a small chip of ruby. Pressure was determined by the ruby-fluorescence method at room temperature (pressure was checked before and after each experiment).[51] The measurements were performed using Quantum Design MPMS-XL7 SQUID magnetometer. Before the actual photomagnetic experiment under pressure, the quality of the sample was checked by recording Raman spectrum and magnetization measurements at ambient pressure.

DOI: 10.1021/jacs.5b04303
J. Am. Chem. Soc. 2015, 137, 8795−8802

■ ASSOCIATED CONTENT

Supporting Information

Additional tables and figures presenting the crystallographic details and magnetic/photomagnetic measurements for **FeNb** and **MnNb**, animation files with structural diagrams, and a video showing the piezochromic effect. The Supporting Information is available free of charge on the ACS Publications website at DOI: 10.1021/jacs.5b04303.

■ AUTHOR INFORMATION

Corresponding Author

*pinkowic@chemia.uj.edu.pl; dawid.pinkowicz@uj.edu.pl

Notes

The authors declare no competing financial interest.

■ ACKNOWLEDGMENTS

This work was supported by the Polish Ministry of Science and Higher Education within the Iuventus Plus Programme (grant agreement no. 0370/IP3/2015/73). D.P. gratefully acknowledges the financial support of the EC REA within the Marie Curie International Outgoing Fellowship, project Multi-CyChem (PIOF-GA-2011-298569). M.M. and K.V.K. would like to acknowledge EP/J00099X and EP/K033646 EPSRC grants. H.T. and A.K. acknowledge the support from the Foundation for Polish Science, grant TEAM 2009-4/6. Magnetic measurements were performed using the equipment purchased from the "Large Research Infrastructure Fund" of the Polish Ministry of Science and Higher Education (contract no. CRZP/UJ/254/2013) and European Regional Development Fund in the framework of the Polish Innovation Economy Operational Program (Project ATOMIN, contract no. POIG.02.01.00-12-023/08).

■ REFERENCES

(1) Bedanta, S.; Petracic, O.; Kleemann, W. Supermagnetism. In *Handbook of Magnetic Materials*, Buschow, K. H. J., Ed. Elsevier: Amsterdam, The Netherlands, 2015; Vol. *23*, pp 1−83.

(2) Yan, S.; Choi, D.-J.; BurgessJacob, A. J.; Rolf-Pissarczyk, S.; Loth, S. *Nat. Nano.* **2015**, *10* (1), 40−45.

(3) Gatteschi, D.; Sessoli, R.; Villain, J. *Molecular Nanomagnets*; OUP: Oxford, 2006.

(4) Komeda, T.; Isshiki, H.; Liu, J.; Zhang, Y.-F.; Lorente, N.; Katoh, K.; Breedlove, B. K.; Yamashita, M. *Nat. Commun.* **2011**, *2*, 217.

(5) Train, C.; Gheorghe, R.; Krstic, V.; Chamoreau, L.-M.; Ovanesyan, N. S.; Rikken, G. L. J. A.; Gruselle, M.; Verdaguer, M. *Nat. Mater.* **2008**, *7*, 729−734.

(6) Train, C.; Gruselle, M.; Verdaguer, M. *Chem. Soc. Rev.* **2011**, *40*, 3297−3312.

(7) Galan-Mascaros, J. R. *Nat. Phys.* **2015**, *11*, 7−8.

(8) Sessoli, R.; Boulon, M.-E.; Caneschi, A.; Mannini, M.; Poggini, L.; Wilhelm, F.; Rogalev, A. *Nat. Phys.* **2015**, *11*, 69−74.

(9) Nishimoto, Y.; Yokogawa, D.; Yoshikawa, H.; Awaga, K.; Irle, S. *J. Am. Chem. Soc.* **2014**, *136*, 9042−9052.

(10) Pointillart, F.; Guennic, B. L.; Golhen, S.; Cador, O.; Maury, O.; Ouahab, L. *Chem. Commun.* **2013**, *49*, 615−617.

(11) Gütlich, P. *Eur. J. Inorg. Chem.* **2013**, *2013*, 581−591.

(12) Matsumoto, T.; Newton, G. N.; Shiga, T.; Hayami, S.; Matsui, Y.; Okamoto, H.; Kumai, R.; Murakami, Y.; Oshio, H. *Nat. Commun.* **2014**, *5*, 3865.

(13) Irie, M.; Fukaminato, T.; Matsuda, K.; Kobatake, S. *Chem. Rev.* **2014**, *114*, 12174−12277.

(14) Risset, O. N.; Quintero, P. A.; Brinzari, T. V.; Andrus, M. J.; Lufaso, M. W.; Meisel, M. W.; Talham, D. R. *J. Am. Chem. Soc.* **2014**, *136*, 15660−15669.

(15) Ababei, R.; Pichon, C.; Roubeau, O.; Li, Y.-G.; Bréfuel, N.; Buisson, L.; Guionneau, P.; Mathonière, C.; Clérac, R. *J. Am. Chem. Soc.* **2013**, *135*, 14840−14853.

(16) Feng, X.; Mathonière, C.; Jeon, I.-R.; Rouzières, M.; Ozarowski, A.; Aubrey, M. L.; Gonzalez, M. I.; Clérac, R.; Long, J. R. *J. Am. Chem. Soc.* **2013**, *135*, 15880−15884.

(17) Mathonière, C.; Lin, H.-J.; Siretanu, D.; Clérac, R.; Smith, J. M. *J. Am. Chem. Soc.* **2013**, *135*, 19083−19086.

(18) Jaffe, A.; Lin, Y.; Mao, W. L.; Karunadasa, H. I. *J. Am. Chem. Soc.* **2015**, *137*, 1673−1678.

(19) Kwon, M. S.; Gierschner, J.; Yoon, S.-J.; Park, S. Y. *Adv. Mater.* **2012**, *24*, 5487−5492.

(20) Ouahab, L. *Multifunctional molecular materials*; CRC Press, Taylor and Francis Group: Boca Raton, FL, 2012.

(21) Pardo, E.; Train, C.; Liu, H.; Chamoreau, L.-M.; Dkhil, B.; Boubekeur, K.; Lloret, F.; Nakatani, K.; Tokoro, H.; Ohkoshi, S.-i.; Verdaguer, M. *Angew. Chem., Int. Ed.* **2012**, *51*, 8356−8360.

(22) Sato, O.; Iyoda, T.; Fujishima, A.; Hashimoto, K. *Science* **1996**, *272*, 704−705.

(23) Verdaguer, M. *Science* **1996**, *272*, 698−699.

(24) Ohkoshi, S.-i.; Imoto, K.; Tsunobuchi, Y.; Takano, S.; Tokoro, H. *Nat. Chem.* **2011**, *3*, 564−569.

(25) Beaulac, R.; Schneider, L.; Archer, P. I.; Bacher, G.; Gamelin, D. R. *Science* **2009**, *325*, 973−976.

(26) Clemente-Leon, M.; Coronado, E.; Lopez-Jorda, M.; Desplanches, C.; Asthana, S.; Wang, H.; Letard, J.-F. *Chem. Sci.* **2011**, *2*, 1121−1127.

(27) Hoshino, N.; Iijima, F.; Newton, G. N.; Yoshida, N.; Shiga, T.; Nojiri, H.; Nakao, A.; Kumai, R.; Murakami, Y.; Oshio, H. *Nat. Chem.* **2012**, *4*, 921−926.

(28) Decurtins, S.; Gütlich, P.; Köhler, C. P.; Spiering, H.; Hauser, A. *Chem. Phys. Lett.* **1984**, *105*, 1−4.

(29) Hauser, A. *Coord. Chem. Rev.* **1991**, *111*, 275−290.

(30) Koumousi, E. S.; Jeon, I.-R.; Gao, Q.; Dechambenoit, P.; Woodruff, D. N.; Merzeau, P.; Buisson, L.; Jia, X.; Li, D.; Volatron, F.; Mathonière, C.; Clérac, R. *J. Am. Chem. Soc.* **2014**, *136*, 15461−15464.

(31) Higel, P.; Villain, F.; Verdaguer, M.; Rivière, E.; Bleuzen, A. *J. Am. Chem. Soc.* **2014**, *136*, 6231−6234.

(32) Wang, X.-Y.; Avendano, C.; Dunbar, K. R. *Chem. Soc. Rev.* **2011**, *40*, 3213−3238.

(33) Pinkowicz, D.; Podgajny, R.; Pelka, R.; Nitek, W.; Balanda, M.; Makarewicz, M.; Czapla, M.; Zukrowski, J.; Kapusta, C.; Zajac, D.; Sieklucka, B. *Dalton Trans.* **2009**, 7771−7777.

(34) Arai, M.; Kosaka, W.; Matsuda, T.; Ohkoshi, S.-i. *Angew. Chem., Int. Ed.* **2008**, *47*, 6885−6887.

(35) Pinkowicz, D.; Pełka, R.; Drath, O.; Nitek, W.; Bałanda, M.; Majcher, A. M.; Poneti, G.; Sieklucka, B. *Inorg. Chem.* **2010**, *49*, 7565−7576.

(36) Prescimone, A.; Milios, C. J.; Moggach, S.; Warren, J. E.; Lennie, A. R.; Sanchez-Benitez, J.; Kamenev, K.; Bircher, R.; Murrie, M.; Parsons, S.; Brechin, E. K. *Angew. Chem., Int. Ed.* **2008**, *47*, 2828−2831.

(37) Parois, P.; Moggach, S. A.; Sanchez-Benitez, J.; Kamenev, K. V.; Lennie, A. R.; Warren, J. E.; Brechin, E. K.; Parsons, S.; Murrie, M. *Chem. Commun.* **2010**, *46*, 1881−1883.

(38) Prescimone, A.; Morien, C.; Allan, D.; Schlueter, J. A.; Tozer, S. W.; Manson, J. L.; Parsons, S.; Brechin, E. K.; Hill, S. *Angew. Chem., Int. Ed.* **2012**, *51*, 7490−7494.

(39) O'Neal, K. R.; Brinzari, T. V.; Wright, J. B.; Ma, C.; Giri, S.; Schlueter, J. A.; Wang, Q.; Jena, P.; Liu, Z.; Musfeldt, J. L. *Sci. Rep.* **2014**, *4*, 6054.

(40) Coronado, E.; Giménez-López, M. C.; Korzeniak, T.; Levchenko, G.; Romero, F. M.; Segura, A.; García-Baonza, V.; Cezar, J. C.; de Groot, F. M. F.; Milner, A.; Paz-Pasternak, M. *J. Am. Chem. Soc.* **2008**, *130*, 15519−15532.

(41) Gütlich, P.; Ksenofontov, V.; Gaspar, A. B. *Coord. Chem. Rev.* **2005**, *249*, 1811−1829.

DOI: 10.1021/jacs.5b04303
J. Am. Chem. Soc. 2015, 137, 8795−8802

(42) Pinkowicz, D.; Kurpiewska, K.; Lewinski, K.; Balanda, M.; Mihalik, M.; Zentkova, M.; Sieklucka, B. *CrystEngComm* **2012**, *14*, 5224−5229.
(43) Ohba, M.; Kaneko, W.; Kitagawa, S.; Maeda, T.; Mito, M. *J. Am. Chem. Soc.* **2008**, *130*, 4475−4484.
(44) Shum, W. W.; Her, J. H.; Stephens, P. W.; Lee, Y.; Miller, J. S. *Adv. Mater.* **2007**, *19*, 2910−2913.
(45) Giriat, G.; Wang, W.; Attfield, J. P.; Huxley, A. D.; Kamenev, K. V. *Rev. Sci. Instrum.* **2010**, *81*, 073905.
(46) Wang, X.; Kamenev, K. V. *Low Temp. Phys.* **2014**, *40*, 735−746.
(47) Carbonera, C.; Dei, A.; Sangregorio, C.; Létard, J.-F. *Chem. Phys. Lett.* **2004**, *396*, 198−201.
(48) Rodríguez-Velamazán, J. A.; Carbonera, C.; Castro, M.; Palacios, E.; Kitazawa, T.; Létard, J.-F.; Burriel, R. *Chem.—Eur. J.* **2010**, *16*, 8785−8796.
(49) Kiernan, P. M.; Griffith, W. P. *J. Chem. Soc., Dalton Trans.* **1975**, 2489−2494.
(50) Merrill, L.; Bassett, W. A. *Rev. Sci. Instrum.* **1974**, *45*, 290−294.
(51) Mao, H. K.; Xu, J.; Bell, P. M. *J. Geophys. Res.: Solid Earth* **1986**, *91*, 4673−4676.
(52) *Xcalibur CCD System, CrysAlisPro Software System*, 1.171.33; Oxford Diffraction Ltd.: Wrocław, Poland, 2009.
(53) Katrusiak, A. *Z. Kristallogr.* **2004**, *219*, 461.
(54) Sheldrick, G. *Acta Crystallogr., Sect. A* **2008**, *64*, 112−122.

DOI: 10.1021/jacs.5b04303
J. Am. Chem. Soc. 2015, 137, 8795−8802